

# Aqueous Stability of Zirconium Clusters, Including the Zr(IV) Hexanuclear Hydrolysis Complex $[\text{Zr}_6\text{O}_4(\text{OH})_4(\text{H}_2\text{O})_{24}]^{12+}$ , from Density Functional Theory

Rebecca D. Stern, Ryan S. Kingsbury, and Kristin A. Persson\*



Cite This: <https://doi.org/10.1021/acs.inorgchem.1c02078>



Read Online

ACCESS |



Metrics & More

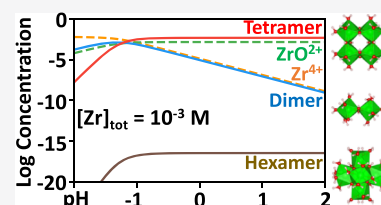


Article Recommendations



Supporting Information

**ABSTRACT:** Framework materials constitute a broad family of solids that range from zeolites and metal–organic frameworks (MOFs) to coordination polymers. The synthesis of such network structures typically rely on precursor molecular building blocks. As an example, the UiO-66 MOF series is constructed of hexanuclear  $[\text{Zr}_6\text{O}_4(\text{OH})_4(\text{CO}_2)_{12}]$  cluster nodes and linear carboxylate linkers. Unfortunately, these Zr MOF cluster nodes cannot currently be manufactured in a sustainable way, motivating a search for “green” alternative synthesis methods. Stabilizing the hexanuclear Zr(IV) cluster (i.e., the hexamer,  $\{\text{Zr}_6^{12+}\}$ ) without the use of organic ligation would enable the use of environmentally friendly solvents such as water. The Zr(IV) tetranuclear cluster (i.e., the tetramer,  $\{\text{Zr}_4^{8+}\}$ ) can be stabilized in solution with or without organic ligands, yet the hexamer has yet to be synthesized without supporting ligands. The reasons why certain zirconium clusters are favored in aqueous solution over others are not well understood. This study reports the relative thermodynamic instability of the hypothetical hexamer  $\{\text{Zr}_6^{12+}\}$  compared to the ubiquitous  $\{\text{Zr}_4^{8+}\}$  tetramer. Density functional theory calculations were performed to obtain the hydrolysis Gibbs free energy of these species and used to construct Zr Pourbaix diagrams that illustrate the effects of electrochemical potential, pH, and Zr(IV) concentration. It was found that the aqueous  $\{\text{Zr}_6^{12+}\}$  hexamer is  $\sim 17.8$  kcal/mol less stable than the aqueous  $\{\text{Zr}_4^{8+}\}$  tetramer at pH = 0, V = 0, and  $[\text{Zr(IV)}] = 1$  M, which is an energy difference on the order of counterion interactions. Electronic structure analyses were used to explore trends in the highest occupied molecular orbital–lowest unoccupied molecular orbital gap, frontier molecular orbitals, and electrostatic potential distribution of these clusters. The evidence suggests that the aqueous  $\{\text{Zr}_6^{12+}\}$  hexamer may be promoted with more strategic syntheses incorporating minimal ligands and counterions.



## INTRODUCTION

Aqueous inorganic metal-oxide clusters occur both naturally and synthetically.<sup>1</sup> They have numerous useful applications in catalysis,<sup>2,3</sup> medicine,<sup>4,5</sup> precursors for thin-film deposition,<sup>6,7</sup> flash memory devices,<sup>8</sup> switchable transparent films,<sup>9</sup> and high-resolution nanopatterning,<sup>10,11</sup> to name a few. These discrete molecular metal oxides can vary in size and geometry, forming coordination complexes that are linked via oxo and hydroxo ligands.<sup>12,13</sup> The examples of metals that have been shown to form metal-oxide clusters include group 5 and 6 polyoxometalates ( $\text{Mo}^{\text{VI}}$ ,  $\text{W}^{\text{VI}}$ ,  $\text{V}^{\text{VI}}$ ,  $\text{Nb}^{\text{V}}$ , and  $\text{Ta}^{\text{V}}$ ),<sup>14,15</sup> other transition metals ( $\text{Fe}^{\text{III}}$ ,  $\text{Cu}^{\text{II}}$ ,  $\text{Zr}^{\text{IV}}$ ,  $\text{Hf}^{\text{IV}}$ , and  $\text{Ti}^{\text{IV}}$ ),<sup>16–25</sup> and post-transition metals ( $\text{Al}^{\text{III}}$ ,  $\text{Ga}^{\text{III}}$ , and  $\text{Sn}^{\text{IV}}$ ).<sup>12,26–28</sup>

Fabricating metal-oxide clusters and cluster-based systems in water offers an environmentally friendly manufacturing approach<sup>1</sup> but often requires adding organic ligands to stabilize the cluster.<sup>18,19</sup> Unfortunately, organic ligands often limit the clusters' applications because they hinder the reactivity or solubility. Hence, developing synthesis procedures to promote metal-oxide cluster formation in an aqueous environment without relying on organic ligands is a key challenge for advancing green chemistry manufacturing.

Aqueous synthesis strategies can be controlled by a number of experimental variables including temperature, metal

concentration, pH, electrochemical potential, and counterions. While the effects of temperature and metal concentration are foreseeable and well understood, the impact of solution characteristics can be complex and interdependent depending on the metal cation.<sup>29</sup> This lack of understanding impedes the ability to fully exploit these control variables to efficiently synthesize new and improved aqueous metal-oxide clusters.

Group 4 metal-oxide clusters comprise a particularly interesting class of materials that are used to build metal–organic frameworks (MOFs)<sup>30,31</sup> for gas storage, catalysis, and drug delivery devices.<sup>23,31,32</sup> MOFs are 3D porous networks made of nodes and linkers.<sup>30,31</sup> However, MOFs are often made with solvothermal synthesis methods that involve high temperatures and organic solvents with harmful byproducts.<sup>33</sup> In order to minimize the use of organic solvents and manufacture at ambient temperature, mechanochemical pathways have been developed such as liquid-assisted grinding.

Received: July 13, 2021

Unfortunately, such methods continue to include complicated reaction steps, use unstable reagents, and often result in amorphous byproducts with a corresponding low yield of the target material.<sup>33–35</sup> Therefore, it is highly desirable to develop sustainable MOF manufacturing methods that occur at ambient temperature and in an aqueous environment. As an example, the famous zirconium-based MOF UiO-66 is constructed of hexanuclear  $[\text{Zr}_6(\mu_3\text{-O})_4(\mu_3\text{-OH})_4(\text{CO}_2)_{12}]$  cluster nodes and linear carboxylate linkers<sup>36</sup> but thus far has been impossible to stabilize in water without organic ligation. Instead, zirconium-oxo clusters hydrolyze and polymerize to the tetranuclear  $[\text{Zr}_4(\mu_2\text{-OH})_8(\text{H}_2\text{O})_{16}]^{8+}$  cluster (i.e.,  $\{\text{Zr}_4^{8+}\}$ ), dominating at low pH.<sup>37–39</sup> The desired hexanuclear  $[\text{Zr}_6(\mu_3\text{-O})_4(\mu_3\text{-OH})_4(\text{H}_2\text{O})_{24}]^{12+}$  cluster containing only water-based ligands (i.e.,  $\{\text{Zr}_6^{12+}\}$ ) remains hypothetical, and the reason for its thermodynamic instability is unclear.

Computational modeling techniques such as density functional theory (DFT) and molecular dynamics (MD) can be used to explore the stability regimes of hypothesized and novel species. For example, DFT and MD were used to investigate aqueous solution effects in polyoxometalates,<sup>40–46</sup> group 13 cations,<sup>12,47,48</sup> the Fe-Keggin,<sup>49</sup> and in modeling the first open-shell Keggin ion.<sup>1</sup> There have been limited computational studies of group 4 metal-oxide clusters, hitherto all using MD techniques.<sup>50–53</sup> Although MD is useful in optimizing the terminal water ligands of aqueous metal clusters, calculating accurate thermodynamic properties (e.g., hydrolysis Gibbs free energies) requires other techniques. In this respect, DFT enables accurate prediction of hydrolysis Gibbs free energies which can then be used to estimate and compare the aqueous stability of different species.<sup>54–57</sup>

Here, we use DFT to investigate the thermodynamic stability of the hypothetical  $\{\text{Zr}_6^{12+}\}$  hexamer in relation to the  $\{\text{Zr}_4^{8+}\}$  tetramer and other Zr(IV) aqueous ions and solids. After optimizing the positions of terminal water ligands using DFT, we calculate the hydrolysis Gibbs free energy of ground-state cluster geometries and use a Pourbaix formalism<sup>58,59</sup> developed for the Materials Project<sup>60</sup> to determine equilibrium constants and electrochemical (E-pH) stability regimes of our modeled species. Auxiliary analyses of the electronic structure alongside electrostatic potential (ESP) maps provide clarity on the thermodynamic landscape governing the competition between the  $\{\text{Zr}_4^{8+}\}$  tetramer and the  $\{\text{Zr}_6^{12+}\}$  hexamer as well as possible avenues for promoting the synthesis of the hexamer. This study is aimed to improve our understanding of the thermodynamic stability relationship between  $\{\text{Zr}_4^{8+}\}$  and  $\{\text{Zr}_6^{12+}\}$  to not only support the efforts to develop green MOF manufacturing but to expand the general knowledge of Zr(IV) aqueous solution chemistry.

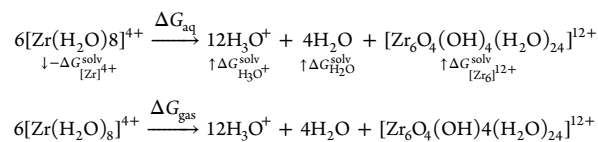
## COMPUTATIONAL DETAILS

(1) The geometry of each cluster was first optimized in vacuum using DFT. Calculations were performed with Gaussian 16<sup>61</sup> software using the B3LYP functional.<sup>62</sup> The basis set 6-31+G(d) was used for oxygen and hydrogen, while the basis set 6-31+G(d) and the associated effective core potential LANL2DZ were used for zirconium.<sup>63–66</sup> A subsequent frequency calculation was performed to verify the absence of imaginary vibration modes to confirm that the system was in a stable/metastable state. The thermal correction to the Gibbs free energy in vacuum was determined from this output, which was added to the computed gas-phase free energy  $\Delta G_{\text{gas}}$ . (2) The geometry was further optimized in

water ( $\epsilon = 78.36$ ) using the continuum solvation model COSMO.<sup>67,68</sup> (3) The electronic energy was refined using the determined optimized geometry in water and using a B3LYP single-point calculation with the basis set 6-311+G(d,p) for oxygen and hydrogen and basis set LANL2DZ for zirconium.<sup>69</sup> The computed gas-phase free energy  $\Delta G_{\text{gas}}$  was determined from this output. (4) The solvation energy was computed using a B3LYP/6-31G(d) single point for oxygen and hydrogen, and a B3LYP/LANL2DZ single point for zirconium. A subsequent single-point calculation with continuum solvation model COSMO was performed with the same functionals and basis sets as the preceding single point. The computed solvation free energy  $\Delta G_{\text{solv}}$  was determined from the outputs as the difference between the energies from the two single-point calculations. Finally, GaussSum was used for orbital analysis.<sup>70</sup> Example input files are provided in Section 5 of the Supporting Information.

## HYDROLYSIS GIBBS FREE ENERGY

A thermodynamic cycle was used to determine the hydrolysis Gibbs free energy,  $\Delta G_{\text{aq}}$ , from computed gas-phase and solvation free energies.<sup>71,72</sup> An example of the thermodynamic cycle for the Zr(IV) hexamer is shown below. The upper reaction is in the aqueous phase and the lower reaction is modeled in vacuum.



The cycles for the dimer and tetramer are provided in Section 3.1 of the Supporting Information. The hydrolysis Gibbs free energy  $\Delta G_{\text{aq}}$  was then determined from

$$\Delta G_{\text{aq}} = \Delta G_{\text{gas}} + \sum_{i=1}^{N_{\text{products}}} n_i \Delta G_i^{\text{solv}} - \sum_{j=1}^{N_{\text{products}}} n_j \Delta G_j^{\text{solv}} \quad (1)$$

## POURBAIX DIAGRAM FORMALISM

The hydrolysis Gibbs free energies are mapped to the Pourbaix formalism<sup>58,59</sup> of the Materials Project.<sup>60</sup> The most important aspect of this formalism is that it uses a combination of computed energies for solid states and clusters with experimental Gibbs free energies for monomeric aqueous ions and water, which means that effects such as aqueous ion solvation are inherently accounted for. The equations and referencing scheme to determine the Pourbaix formalism energy  $\Delta G_{\text{pourbaix}}$  from the hydrolysis Gibbs free energy  $\Delta G_{\text{aq}}$  are shown in Section 3.2 of the Supporting Information

## CODE AVAILABILITY

The code to plot Pourbaix diagrams is available via pymatgen: [https://github.com/materialsproject/pymatgen/blob/master/pymatgen/analysis/pourbaix\\_diagram.py](https://github.com/materialsproject/pymatgen/blob/master/pymatgen/analysis/pourbaix_diagram.py)<sup>54,58,59,73</sup>

## RESULTS AND DISCUSSION

**Structures.** The computed DFT ground-state structure of the zirconium tetramer  $[\text{Zr}_4(\text{OH})_8(\text{H}_2\text{O})_{16}]^{8+}$  is shown in Figure 1a. The tetramer has four  $\text{Zr}^{4+}$  ions, each 8-coordinate with distorted square antiprism geometry. These four Zr(IV) building units are bonded by double  $\text{OH}^-$  bridges. Therefore,

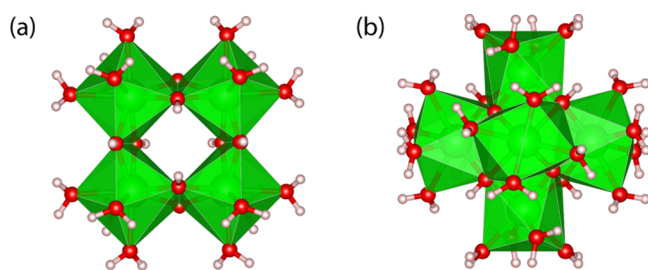


**Figure 1.** (a) Ground-state geometry of the zirconium(IV) tetranuclear species  $[\text{Zr}_4(\text{OH})_8(\text{H}_2\text{O})_{16}]^{8+}$ . (b) Ground-state geometry of the zirconium(IV) hexanuclear species  $[\text{Zr}_6\text{O}_4(\text{OH})_4(\text{H}_2\text{O})_{24}]^{12+}$ . Green polyhedra: zirconium. Red: oxygen. White: hydrogen.

one  $\text{Zr}^{4+}$  ion is connected to four  $\text{OH}^-$  and four  $\text{H}_2\text{O}$  ligands. These four building units form a planar square with respect to the zirconium ions. The computed bond lengths and angles for the tetranuclear zirconium cluster compare well to the EXAFS experimental data and solution-phase computational data (see Table S3).<sup>50,74</sup>

We also report, for the first time, the DFT-relaxed structure for the hypothetical zirconium hexamer  $[\text{Zr}_6\text{O}_4(\text{OH})_4(\text{H}_2\text{O})_{24}]^{12+}$  (Figure 1b). The hexamer exhibits  $\text{Zr}(\text{IV})$  building units like the tetramer, being 8-coordinate in a distorted square antiprism fashion. However, the six  $\text{Zr}^{4+}$  ions are bonded to two  $\text{O}^{2-}$ , two  $\text{OH}^-$ , and four terminal  $\text{H}_2\text{O}$  ligands each. These six units form a compact structure similar to the hexanuclear acetate complex reported by Hennig et al.<sup>75</sup> The computed bond lengths and angles for the hexanuclear zirconium clusters are similar to those of the hexanuclear  $\text{Zr}(\text{IV})$  acetate complex in an aqueous solution of 0.1 M  $\text{Zr}(\text{IV})$  in 1 M acetic acid at pH 1.5 as reported by Hennig et al. (see Table S4).<sup>75</sup>

The computed DFT ground-state structure of the zirconium monomer  $[\text{Zr}(\text{H}_2\text{O})_8]^{4+}$  (i.e.,  $\{\text{Zr}^{4+}\}$ ) and dimer

$[\text{Zr}_2(\text{OH})_2(\text{H}_2\text{O})_{12}]^{6+}$  (i.e.,  $\{\text{Zr}_2^{6+}\}$ ) is depicted in Figures S1 and S2, respectively. The monomer exhibits a classic square antiprism geometry, with a  $\text{Zr}^{4+}$  center bound to eight water ligands, while the dimer has a slightly distorted square antiprism geometry, with two 8-coordinate  $\text{Zr}^{4+}$  ions connected to two  $\text{OH}^-$  and six  $\text{H}_2\text{O}$  ligands. The monomer and dimer's bond lengths and angles are listed in Tables S1 and S2, respectively. These values are comparable to the experimental and computationally reported results.<sup>51,74</sup>

**Pourbaix Diagrams.** The calculated hydrolysis Gibbs free energies  $\Delta G_{\text{aq}}$  of the dimer, tetramer, and hexamer are  $-6.4$ ,  $-23.4$ , and  $-17.5$  kcal/mol, respectively (Table S6). At first glance, the low hydrolysis Gibbs free energy of the tetramer indicates that the tetramer is the most stable configuration. However, including the cluster free energies (correctly referenced, see Section 3.2 of the Supporting Information) on the Zr Pourbaix diagram with respect to other aqueous ions and solids (Figure 2) allows for a more nuanced understanding that includes the effects of electrochemical potential, pH, and  $\text{Zr}(\text{IV})$  concentration.

At a zirconium concentration of  $10^{-4}$  M, the aqueous zirconium ion  $\text{Zr}^{4+}$  and the zirconyl ion  $\text{ZrO}^{2+}$  are stable at low pH values, as shown in Figure 2a. Increasing the concentration to  $[\text{Zr}(\text{IV})] = 10^{-3}$  M, the dimer and tetramer outcompete  $\text{ZrO}^{2+}$ , as is illustrated in Figure 2b. This stability prediction is consistent with experimental observations that  $\text{Zr}(\text{IV})$  has a strong tendency to hydrolyze and polymerize for  $[\text{Zr}(\text{IV})] > 10^{-4}$  M at low pH.<sup>75</sup> As the zirconium concentration is increased further to  $10^{-2}$  and  $10^{-1}$  M, the tetramer develops a broader stability window in the direction of lower pH (Figure 2c,d). This stability prediction is specifically comparable to the experimental results reported by Hennig et al.,<sup>75</sup> which observes the tetramer at pH = 1.5 when  $[\text{Zr}(\text{IV})] = 10^{-1}$  M. These results can also be seen from the speciation diagrams presented in Figure 3. As the Zr concentration increases, the species with the highest concentration changes (as indicated by the species with a log concentration closest to zero). The

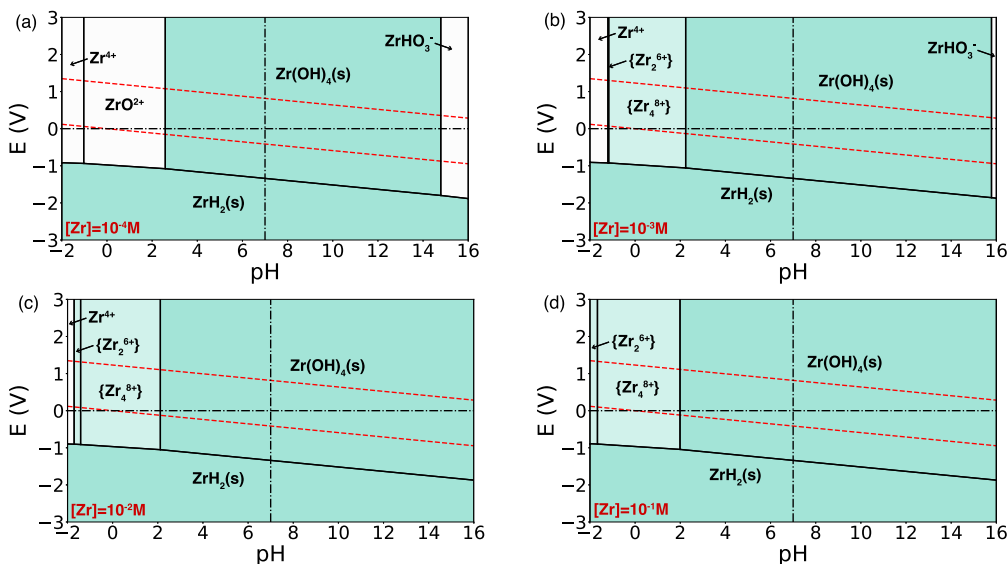


**Figure 2.** Zirconium Pourbaix diagrams at varying  $[\text{Zr}(\text{IV})]$  concentrations. (a)  $[\text{Zr}(\text{IV})] = 10^{-4}$  M,  $\text{ZrO}^{2+}$  is between  $-1.0 \leq \text{pH} \leq 2.5$ . (b)  $[\text{Zr}(\text{IV})] = 10^{-3}$  M,  $\{\text{Zr}_2^{6+}\}$  is at  $\text{pH} = -1.2$ ,  $\{\text{Zr}_4^{8+}\}$  is between  $-1.1 \leq \text{pH} \leq 2.2$ . (c)  $[\text{Zr}(\text{IV})] = 10^{-2}$  M,  $\{\text{Zr}_2^{6+}\}$  is between  $-1.7 \leq \text{pH} \leq -1.5$ ,  $\{\text{Zr}_4^{8+}\}$  is between  $-1.4 \leq \text{pH} \leq 2.1$ . (d)  $[\text{Zr}(\text{IV})] = 10^{-1}$  M,  $\{\text{Zr}_2^{6+}\}$  is between  $-2.0 \leq \text{pH} \leq -1.7$ ,  $\{\text{Zr}_4^{8+}\}$  is between  $-1.6 \leq \text{pH} \leq 1.9$ . Note: Dimer,  $\{\text{Zr}_2^{6+}\} = [\text{Zr}_2(\text{OH})_2(\text{H}_2\text{O})_{12}]^{6+}$ . Tetramer,  $\{\text{Zr}_4^{8+}\} = [\text{Zr}_4(\text{OH})_8(\text{H}_2\text{O})_{16}]^{8+}$ . Hexamer,  $\{\text{Zr}_6^{12+}\} = [\text{Zr}_6\text{O}_4(\text{OH})_4(\text{H}_2\text{O})_{24}]^{12+}$ .  $\text{Zr}(\text{OH})_4$  is hydrated oxide  $\text{ZrO}_2 \cdot 2\text{H}_2\text{O}$ .

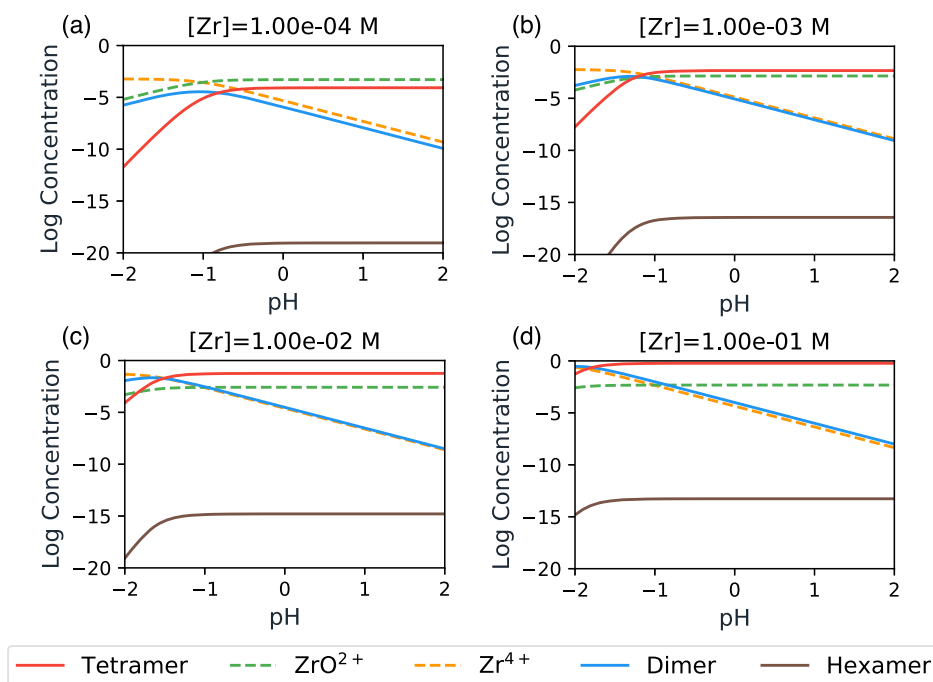


**Figure 3.** Zirconium speciation diagrams at varying  $[Zr(IV)]$  concentrations corresponding to those shown in Figure 2 and a potential of 0 V. A log concentration closer to zero indicates a large concentration of that species. (a)  $Zr^{4+}$  to  $ZrO^{2+}$  transition at  $pH = -1.0$ . (b)  $Zr^{4+}$  to Zr dimer transition at  $pH = -1.2$ , Zr dimer to Zr tetramer transition at  $pH = -1.1$ . (c)  $Zr^{4+}$  to Zr dimer transition at  $pH = -1.7$ , Zr dimer to Zr tetramer transition at  $pH = -1.5$ . (d) Zr dimer to Zr tetramer transition at  $pH = -1.7$ .

**Table 1. Equilibrium Reactions, Energies, and Constants**

equilibrium species	equilibrium reaction	$\Delta G_{rxn}^{\circ}$ (kJ/mol)	$\log(K^{\circ})$
(a) monomer/tetramer	$4Zr^{4+} + 24H_2O = 8H^+ + [Zr_4(OH)_8(H_2O)_{16}]^{8+}$	-98.07	$17.19 = \log \frac{[Zr_4^{8+}]}{[Zr^{4+}]^4} - 8 \text{ pH}$
(b) dimer/tetramer	$2[Zr_2(OH)_2(H_2O)_{12}]^{6+} = 4H^+ + 4H_2O + [Zr_4(OH)_8(H_2O)_{16}]^{8+}$	-44.40	$7.78 = \log \frac{[Zr_4^{8+}]}{[Zr_2^{6+}]^2} - 4 \text{ pH}$
(c) monomer/dimer	$2Zr^{4+} + 14H_2O = 2H^+ + [Zr_2(OH)_2(H_2O)_{12}]^{6+}$	-26.83	$4.70 = \log \frac{[Zr_2^{6+}]}{[Zr^{4+}]^2} - 2 \text{ pH}$
(d) $ZrO^{2+}$ /tetramer	$4ZrO^{2+} + 20H_2O = [Zr_4(OH)_8(H_2O)_{16}]^{8+}$	-51.79	$9.08 = \log \frac{[Zr_4^{8+}]}{[ZrO^{2+}]^4}$
(e) monomer/hexamer	$6Zr^{4+} + 32H_2O = 12H^+ + [Zr_6O_4(OH)_4(H_2O)_{24}]^{12+}$	-73.33	$12.85 = \log \frac{[Zr_6^{12+}]}{[Zr^{4+}]^6} - 12 \text{ pH}$
(f) dimer/hexamer	$3[Zr_2(OH)_2(H_2O)_{12}]^{6+} = 6H^+ + 10H_2O + [Zr_6O_4(OH)_4(H_2O)_{24}]^{12+}$	7.17	$-1.26 = \log \frac{[Zr_6^{12+}]}{[Zr_2^{6+}]^3} - 6 \text{ pH}$
(g) $ZrO^{2+}$ /hexamer	$6ZrO^{2+} + 26H_2O = [Zr_6O_4(OH)_4(H_2O)_{24}]^{12+}$	-3.90	$0.68 = \log \frac{[Zr_6^{12+}]}{[ZrO^{2+}]^6}$
(h) tetramer/hexamer	$3[Zr_4(OH)_8(H_2O)_{16}]^{8+} = 8H_2O + 2[Zr_6O_4(OH)_4(H_2O)_{24}]^{12+}$	147.55	$-25.86 = \log \frac{[Zr_6^{12+}]^2}{[Zr_4^{8+}]^3}$
(i) monomer/ $ZrO^{2+}$	$Zr^{4+} + H_2O = 2H^+ + ZrO^{2+}$	-11.57	$2.03 = \log \frac{[ZrO^{2+}]}{[Zr^{4+}]} - 2 \text{ pH}$

species with the highest concentration at that pH is also the species that appears on the respective Pourbaix diagram at that pH.

From our calculated Pourbaix formalism energies  $\Delta G_{\text{pourbaix}}$  reported in Table S6, we calculated the equilibrium constants ( $K^{\circ}$ ) for various reactions between the monomer,  $ZrO^{2+}$ , dimer, tetramer, and hexamer, using the equations in Section 3.3 of the Supporting Information. Our calculated equilibrium

constants indicate that the tetramer is the cluster that is most likely to form from either monomers or dimers (Table 1). Our calculated  $\log(K^{\circ})$  value for the equilibrium reaction involving four monomers forming the tetramer is 17.19. In addition, for the reaction describing two dimers joining to form the tetramer, we obtain  $\log(K^{\circ}) = 7.78$ . Last,  $\log(K^{\circ})$  is calculated to be 4.70 for the reaction of two  $Zr^{4+}$  combining to the dimer. These three large positive calculated  $\log(K^{\circ})$  values suggest

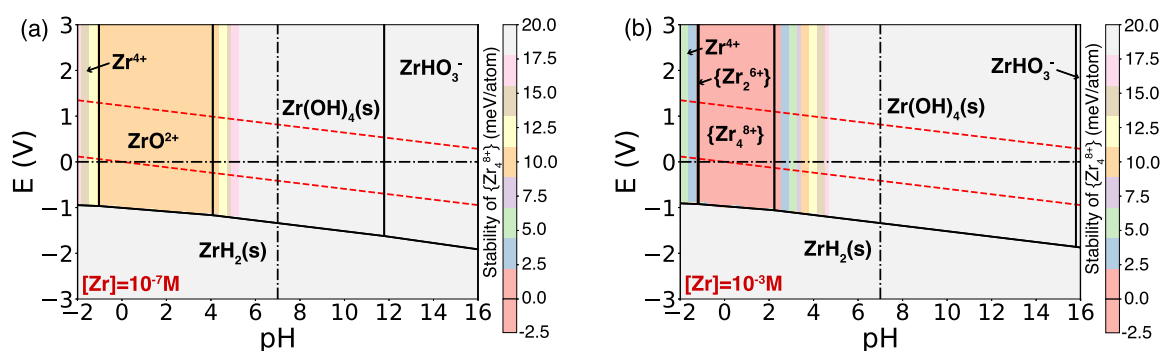


**Figure 4.** Zirconium Pourbaix diagrams at two different  $[\text{Zr(IV)}]$  concentrations, superimposed with heat maps which indicate the relative stability of the tetramer  $\{\text{Zr}_4^{8+}\}$  compared to each stable species. (a)  $[\text{Zr(IV)}] = 10^{-7}$  M showing that the tetramer is 10 meV/atom less stable than  $\text{ZrO}^{2+}$ . (b)  $[\text{Zr(IV)}] = 10^{-3}$  M showing that the tetramer is 1 meV/atom more stable than  $\text{ZrO}^{2+}$ . Note: Dimer,  $\{\text{Zr}_2^{6+}\} = [\text{Zr}_2(\text{OH})_2(\text{H}_2\text{O})_{12}]^{6+}$ . Tetramer,  $\{\text{Zr}_4^{8+}\} = [\text{Zr}_4(\text{OH})_8(\text{H}_2\text{O})_{16}]^{8+}$ .  $\text{Zr}(\text{OH})_4$  is hydrated oxide  $\text{ZrO}_2 \cdot 2\text{H}_2\text{O}$ .

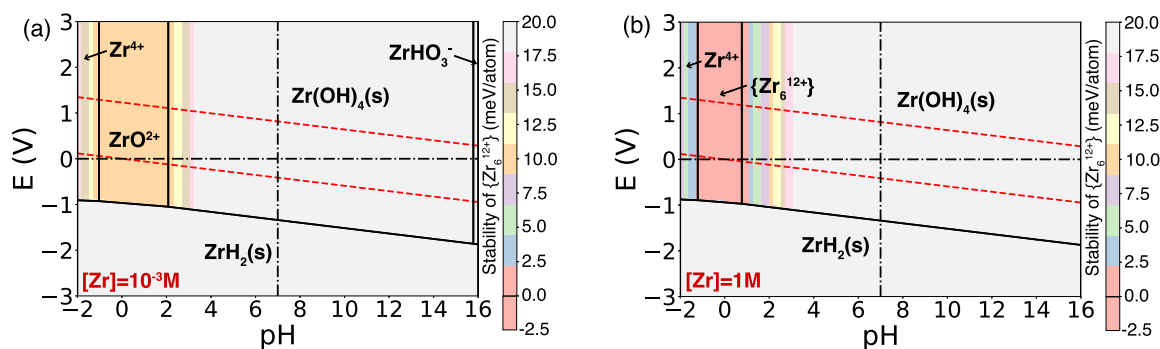


**Figure 5.** Zirconium Pourbaix diagrams at two different  $[\text{Zr(IV)}]$  concentrations, superimposed with heat maps which indicate the relative stability of the hexamer  $\{\text{Zr}_6^{12+}\}$  compared to each stable species (excluding the dimer and tetramer which have been removed from this plot to simulate a scenario where these two species are kinetically inhibited to nucleate). (a)  $[\text{Zr(IV)}] = 10^{-3}$  M, showing that the hexamer is 9 meV/atom less stable than  $\text{ZrO}^{2+}$ . (b)  $[\text{Zr(IV)}] = 1$  M, showing that the hexamer is 1 meV/atom more stable than  $\text{ZrO}^{2+}$ . Note: Hexamer,  $\{\text{Zr}_6^{12+}\} = [\text{Zr}_6\text{O}_4(\text{OH})_4(\text{H}_2\text{O})_{24}]^{12+}$ .  $\text{Zr}(\text{OH})_4$  is hydrated oxide  $\text{ZrO}_2 \cdot 2\text{H}_2\text{O}$ .

that monomers and dimers readily produce the tetramer in large yields. It has been experimentally observed that the Zr tetramer can also form an octameric cluster made of two stacked tetramers bridged by hydroxyl ligands.<sup>76</sup> We were unable to simulate this structure; however, the experimental  $\log(K^\circ)$  value is  $-0.7$ , indicating that formation of this species is thermodynamically unfavorable compared to the tetramer.

Heat maps illustrating the relative stability of Zr species on the Pourbaix diagrams are shown in Figures 4–6. In the heat maps, the color indicates the stability of one selected unstable species (labeled vertically beside the color key) relative to the stable species labeled within each domain of the Pourbaix diagram. For example, Figure 4 shows the free energy of the tetramer  $\{\text{Zr}_4^{8+}\}$  relative to competing (stable) species  $\text{Zr}^{4+}$ ,  $\text{ZrO}^{2+}$ ,  $\text{Zr}(\text{OH})_4$ ,  $\text{ZrHO}_3^-$ , and  $\text{ZrH}_2$ . It is clear that  $\text{ZrO}^{2+}$  and the tetramer compete for the same stability regime (i.e., same region of potential–pH space) on the Zr Pourbaix diagram, according to the color code. To illustrate the increasing stability of the tetramer with concentration, Figure 4a,b shows the stability of the tetramer relative to each species for  $[\text{Zr(IV)}]$  of  $10^{-7}$  and  $10^{-3}$  M, respectively. Figure 4b shows how a total Zr concentration of  $10^{-3}$  M stabilizes the tetramer over  $\text{ZrO}^{2+}$ . The energy difference between the tetramer and  $\text{ZrO}^{2+}$  decreases from 10 to  $-1$  meV/atom as the concentration increases, such that the tetramer becomes the stable species at  $[\text{Zr(IV)}] = 10^{-3}$  M. Specifically, the total Zr concentration must be greater than  $9.4 \times 10^{-4}$  M in order for the tetramer to be promoted over  $\text{ZrO}^{2+}$ , as can be calculated

by solving reaction (d) in Table 1 for when the concentration of the two species are equivalent.

Similarly, the  $\text{ZrO}^{2+}$  species and the hexamer compete for the same stability regime. To better visualize the equilibrium boundary between  $\text{Zr}^{4+}$  and the hexamer, we removed the dimer and the tetramer from the cluster dataset to simulate a scenario where the dimer and tetramer are kinetically inhibited from nucleating. Furthermore, the calculated  $\log(K^\circ)$  for three dimers combining to form the hexamer,  $\log(K^\circ) = -1.26$ , indicates that this reaction is unlikely. Although we were unable to simulate a trimeric zirconium cluster, a  $\log(K^\circ)$  value of 0.4 has been experimentally reported for three monomers forming a trimer.<sup>77</sup> Therefore, we expect that most likely the building blocks of the hexamer are six monomers since our predicted  $\log(K^\circ)$  is 12.85. In this kinetically limited scenario, heat maps in Figure 5 show the relative stability of the hexamer  $\{\text{Zr}_6^{12+}\}$  with all the other species, excluding the dimer and tetramer. Upon systematically increasing the zirconium concentration, we find that an increase in  $[\text{Zr(IV)}]$  from  $10^{-3}$  to 1 M decreases the energy difference between the hexamer and  $\text{ZrO}^{2+}$  from 9 to  $-1$  meV/atom, such that the hexamer became the stable species at  $[\text{Zr(IV)}] = 1$  M, as shown in the heat maps in Figure 5a,b. In fact, the total Zr concentration must be greater than  $7.3 \times 10^{-1}$  M in order for the hexamer to be promoted over  $\text{ZrO}^{2+}$ , as can be calculated by solving reaction (g) in Table 1 for when the concentration of the two species are equivalent.

Finally, the heat map in Figure 6 shows the relative stability of the hexamer  $\{\text{Zr}_6^{12+}\}$  with all the other species, including the

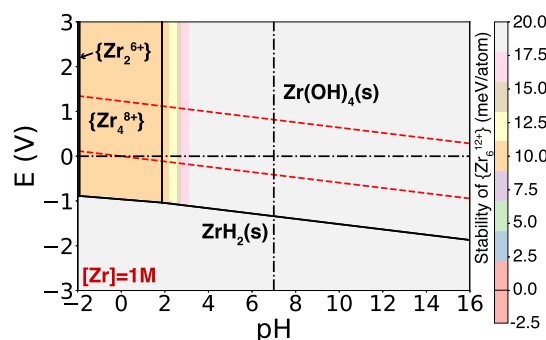


**Figure 6.** Zirconium Pourbaix diagram at  $[\text{Zr(IV)}] = 1 \text{ M}$ , superimposed with a heat map which indicates the relative stability of the hexamer  $\{\text{Zr}_6^{12+}\}$  compared to each stable species. This figure shows that the hexamer is 9 meV/atom less stable than the tetramer. Note: Dimer,  $\{\text{Zr}_2^{6+}\} = [\text{Zr}_2(\text{OH})_2(\text{H}_2\text{O})_{12}]^{6+}$ . Tetramer,  $\{\text{Zr}_4^{8+}\} = [\text{Zr}_4(\text{OH})_8(\text{H}_2\text{O})_{16}]^{8+}$ . Hexamer,  $\{\text{Zr}_6^{12+}\} = [\text{Zr}_6\text{O}_4(\text{OH})_4(\text{H}_2\text{O})_{24}]^{12+}$ .  $\text{Zr}(\text{OH})_4$  is hydrated oxide  $\text{ZrO}_2 \cdot \text{H}_2\text{O}$ .

dimer and tetramer. It is clear that the tetramer and the hexamer compete for the same stability regime, yet an increase in Zr concentration is not able to provide enough thermodynamic driving force for the hexamer to outcompete the tetramer. We find no attainable Zr concentration for which the hexamer is more stable than the tetramer. To this end, the heat map shown in Figure 6 at  $[\text{Zr(IV)}] = 1 \text{ M}$  looks quite similar to the various heat maps at other Zr concentrations, indicating that an energy difference of about 9 meV/atom between the hexamer and tetramer cannot be overcome by simply changing the concentration of zirconium.

The effects of concentration on the relative stability of species, at the same pH and potential, is ultimately determined by their stoichiometry.  $\text{ZrO}^{2+}$  requires only one zirconium ion to form, whereas  $\{\text{Zr}_6^{12+}\}$  requires six (see reactions (i) and (e) in Table 1). As a result, a 3 order of magnitude increase in  $[\text{Zr(IV)}]$  provides enough thermodynamic driving force for the hexamer to outcompete the zirconyl ion. By comparison, a 4 order of magnitude increase in  $[\text{Zr(IV)}]$  is needed for the 4:1 ratio of zirconium ions required to form  $\{\text{Zr}_4^{8+}\}$  (see reaction (a) in Table 1). By contrast, for the case of  $\{\text{Zr}_4^{8+}\}$  and  $\{\text{Zr}_6^{12+}\}$ , three tetramers are consumed to form two hexamers, and therefore, increasing the zirconium concentration has less of an impact on their relative stability. All calculated energy differences for  $[\text{Zr(IV)}]$  ranging from  $10^{-7}$  to 1 M are reported in Table S11. This study has assumed unit activity coefficients for all species. Although using exact activity coefficients (were they available) would alter the values of the equilibrium constants somewhat (particularly at high total  $[\text{Zr(IV)}]$  concentrations), the difference in stability between the tetramer and hexamer is sufficiently large that a change in Zr activity will not provide enough driving force to promote the hexamer over the tetramer.

For the hexamer with 90 total atoms and 6 Zr(IV) ions, this 9 meV/atom energy difference between the hexamer and tetramer at  $\text{pH} = 0$ ,  $V = 0$ , and  $[\text{Zr(IV)}] = 1 \text{ M}$  is  $\sim 129 \text{ meV/Zr}$  or  $\sim 17.8 \text{ kcal/mol}$ . If the activity coefficients for the tetramer and hexamer were available, we estimate that the hexamer could be 16.2–20.6 kcal/mol less stable than the tetramer (see Section 3.3.1 of the Supporting Information).

We note that this energy difference is comparable to experimentally observed energy differences between other metal-oxo cluster polymorphs. For example, a flat- $[\text{Al}_{13}(\text{OH})_{24}(\text{H}_2\text{O})_{24}]^{15+}$  Keggin ion is only about  $\sim 9 \text{ kcal/mol}$  less stable than an  $\epsilon$ - $[\text{Al}_{13}\text{O}_4(\text{OH})_{24}(\text{H}_2\text{O})_{12}]^{7+}$  Keggin ion, as reported by Wills et al., yet the flat- $[\text{Al}_{13}]$  Keggin ion has been synthesized by Wang et al., using additional zinc in solution.<sup>12,78</sup> Wills et al. further claim that the  $[\text{Ga}_{13}\text{O}_4(\text{OH})_{24}(\text{H}_2\text{O})_{12}]^{7+}$  Keggin ion, which has not yet been synthesized, is less stable than the monomeric aqueous specie  $[\text{Ga}(\text{OH})_2]^+$  by  $\sim 21 \text{ kcal/mol}$ , observing that these energy ranges are on the order of counterion interactions.<sup>12,29</sup> Therefore, we hypothesize that since the energy difference between the tetramer and hexamer is also on the order of counterion interactions at  $\sim 17.8 \text{ kcal/mol}$  at  $\text{pH} = 0$ ,  $V = 0$ , and  $[\text{Zr(IV)}] = 1 \text{ M}$ , the Zr(IV) hexamer could be synthesized with proper selection of counterions.

**Electronic Structure Analysis.** To explore the electronic structure and correlate it with the instability of the Zr(IV) hexamer, we calculated the HOMO (highest occupied molecular orbital)–LUMO (lowest unoccupied molecular orbital) gaps (Table 2). We find that for the monomer,

**Table 2.** HOMO and LUMO Energies and Gaps for Selected Zirconium Clusters in eV

species	formula	HOMO	LUMO	Gap
monomer	$[\text{Zr}(\text{H}_2\text{O})_8]^{4+}$	-10.92	-4.05	6.87
hexamer	$[\text{Zr}_6\text{O}_4(\text{OH})_4(\text{H}_2\text{O})_{24}]^{12+}$	-10.37	-3.63	6.74
dimer	$[\text{Zr}_2(\text{OH})_2(\text{H}_2\text{O})_{12}]^{6+}$	-10.21	-3.60	6.62
tetramer	$[\text{Zr}_4(\text{OH})_8(\text{H}_2\text{O})_{16}]^{8+}$	-9.41	-2.97	6.43

dimer, and tetramer, as the size of the cluster decreases, the HOMO–LUMO gap increases, consistent with quantum confinement effects.<sup>79</sup> In contrast, the hexamer deviates from this trend. Visualizing the frontier molecular orbitals (FMOs), it is clear that the HOMO of the monomer, dimer, tetramer, and hexamer are all centered on the oxygen atoms (Figures S3b, 7b, 8b, and 9b, respectively). However, for the hexamer, the fractional contribution to its HOMO is 11% zirconium and 89% oxygen and hydrogen. On the other hand, the dimer's fractional contribution to its HOMO is 7% zirconium and 93% oxygen and hydrogen, and the tetramer's fractional contribution to its HOMO is 4% zirconium and 96% oxygen and hydrogen. Therefore, the greater orbital overlap between the Zr and the O and H atoms lowers the hexamer's HOMO energy below that of the dimer and tetramer.

The LUMO of the monomer is dominated by the Zr d-orbital, following the basic square antiprismatic crystal field splitting (LUMO as  $d_z^2$ , then  $d_{xy}$  and  $d_{x^2-y^2}$ , then  $d_{xz}$  and  $d_{yz}$ ) (Figure S3c). As the clusters grow in size, the complexity of the crystal field splitting increases. The dimer and tetramer's LUMOs are similar to one another in that the d-orbitals centered on each Zr ( $d_{xz}$  and  $d_{x^2-y^2}$ , respectively) are aligned parallel to one another, but with their phases oriented to minimize the overlap (Figure 7c and 8c, respectively). In contrast, the LUMO for the hexamer is degenerate with its LUMO + 1, and the d-orbitals centered on each Zr ( $d_{x^2-y^2}$  type) are aligned perpendicular for neighboring Zr such that there is a greater orbital overlap (Figure 9c). For the hexamer, we calculate the fractional contribution to its LUMO to be 94% zirconium and 6% oxygen and hydrogen. On the other hand, the dimer's fractional contribution to its LUMO is 93%

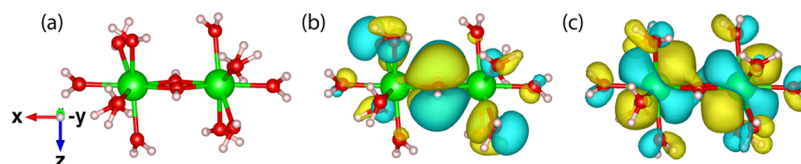


Figure 7. FMOs for Zr(IV) dimer. (a) Dimer structure. (b) HOMO. (c) LUMO.

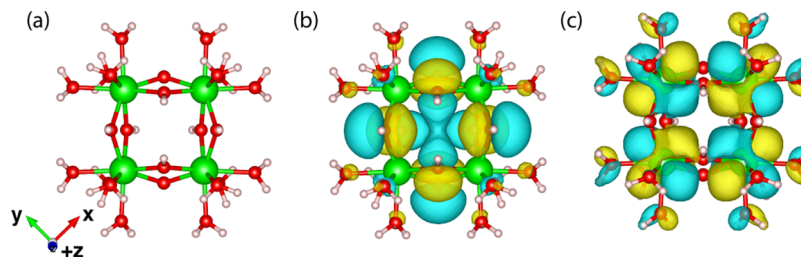


Figure 8. FMOs of the Zr(IV) tetramer. (a) Tetramer structure. (b) HOMO. (c) LUMO.

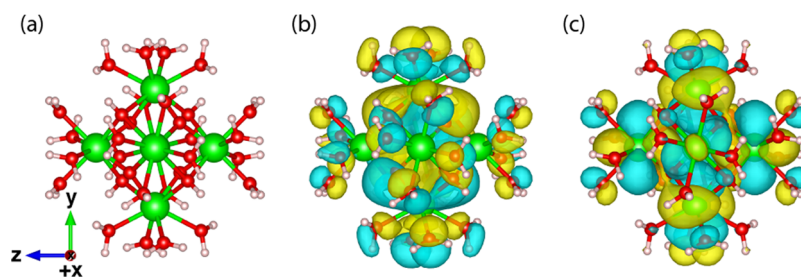


Figure 9. FMOs of the Zr(IV) hexamer. (a) Hexamer structure. (b) HOMO. (c) LUMO.

zirconium and 7% oxygen and hydrogen, and the tetramer's fractional contribution to its LUMO is 96% zirconium and 4% oxygen and hydrogen. The hexamer and dimer are similar in their LUMO fractional contributions, hence their similar LUMO energies. The slightly larger orbital overlap between the Zr and the O and H atoms in the hexamer's LUMO compared to that of the tetramer is reflected in the hexamer's lower LUMO energy.

**ESP Maps.** As noted above, the difference in hydrolysis Gibbs free energy between the Zr tetramer and hexamer is on the order of counterion effects. Since we did not explicitly include counterions in this study, we generated ESP maps to show the charge distribution in the modeled clusters as a way of estimating how counterions might affect the Zr cluster stability. The regions of dense blue (more positive) charge may guide speciation and placement of counteranions, potentially improving the stability of the cationic Zr(IV) clusters in solution.

At first glance, the ESP map of the tetramer (Figure 10a) exhibits many blue regions, but noting the location of  $\text{Cl}^-$  counteranions observed in the literature,<sup>37–39</sup> we know that the counterions tend to wrap along the perimeter of the tetramer. Therefore, we rotated the tetramer to face the side (Figure 10b,c). Examining the alternation of blue regions from the right of the bridging oxygen (Figure 10b) to the left of the bridging oxygen (image not shown) as the tetramer is rotated, we observe four deep blue locations at the bridging oxygen location. Additionally, when viewing the tetramer from the side with the top of a Zr ion at the center (Figure 10c), we count four deep blue locations at a diagonal on top of the Zr ion. The eight total highly positive charged regions are situated along the perimeter of the tetramer, allowing eight counterions, for

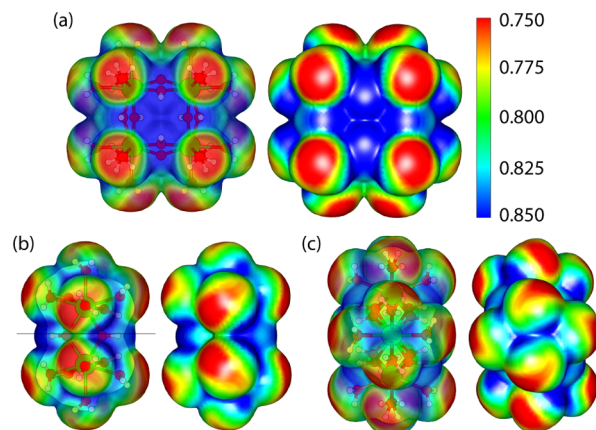


Figure 10. ESP map of the Zr(IV) tetramer, isosurface level = 0.001. (a) Front view. (b) Side bridging oxygen view. (c) Side top of zirconium view.

example  $\text{Cl}^-$ , to reside, thus neutralizing the overall charge of the  $\{\text{Zr}_4^{8+}\}$  tetramer.

Inspecting the ESP map of the hexamer, we again observe eight very dark blue regions: four seen in Figure 11 and four mirror sites in the back of the hexamer. Assuming that the site availability limits the  $\{\text{Zr}_6^{12+}\}$  hexamer to eight total  $\text{Cl}^-$  counteranions, it can only reduce its charge to 4+. Hence, although the energy difference between the tetramer and the hexamer is on the order of counterion interactions, the hexamer may be unable to improve its competitiveness through counterion interactions, as compared with the tetramer. We note that the experimentally synthesized Zr(IV) hexamer nodes used to form the UiO-66 family of MOFs

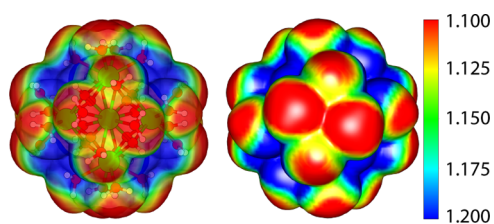


Figure 11. ESP map of the Zr(IV) hexamer, isosurface level = 0.001.

require syntheses with sulfate counterions and glycine ligands,<sup>80</sup> or acetic acid ligands/modulators,<sup>33,75,81</sup> or dimethylformamide (DMF) and HCl solutions.<sup>82</sup> These higher charged counterions and/or bulky ligands may be required in order to favor the geometry of the hexamer over that of the tetramer.

From the monomer's ESP map in Figure S4, we note four regions of deep blue intensity at the posterior triangular faces. We hypothesize that four counteranions, such as  $\text{Cl}^-$ , could occupy these sites and neutralize the  $\{\text{Zr}^{4+}\}$  monomer. In the ESP map of the dimer, it appears that there are four dark blue regions around the bridging hydroxyl ligands (Figure S5). If the  $\{\text{Zr}_2^{6+}\}$  dimer can only accommodate four  $\text{Cl}^-$  counteranions, its overall 6+ charge would be lowered to 2+.

In summary, the first-principles calculated structural characteristics and stability trends we obtain for the aqueous Zr(IV) dimer, tetramer, and hexamer match experimental observations in three main ways. First, the dimer  $[\text{Zr}_2(\text{OH})_2(\text{H}_2\text{O})_{12}]^{6+}$  exhibits small stability windows in Eh-pH diagrams and is often overpowered by the tetramer. Second, the tetramer  $[\text{Zr}_4(\text{OH})_8(\text{H}_2\text{O})_{16}]^{8+}$  is shown as the predominant cluster in an aqueous environment at low pH and relatively low concentrations of Zr. Third, the hexamer  $[\text{Zr}_6\text{O}_4(\text{OH})_4(\text{H}_2\text{O})_{24}]^{12+}$  could not be stabilized at any concentration of Zr or pH, albeit neglecting any potential stabilizing effects of counterions or bulky supporting ligands.

## SUMMARY AND OUTLOOK

To improve our understanding of aqueous zirconium chemistry and advance more sustainable synthesis strategies for functional metal-oxide clusters, we used density functional theory to investigate the thermodynamic stability of known, as well as hypothetical Zr clusters (tetramer and hexamer, respectively). We analyzed Zr Pourbaix diagrams to show that the tetramer is more stable than the hexamer for all reasonable pH and potential values in alignment with experimental observations. However, Gibbs free energies of the hexamer relative to the tetramer (9 meV/atom or  $\sim 17.8$  kcal/mol at pH = 0,  $V = 0$ , and  $[\text{Zr}(\text{IV})] = 1$  M) were found to be within the range of counterion effects. An electronic structure analysis revealed that while the monomer, dimer, and tetramer HOMO–LUMO gaps follow quantum confinement trends, the hexamer does not. We find that the HOMO of the hexamer exhibits a greater orbital overlap between the Zr and the O and H atoms as compared to the dimer or tetramer, which decreases the energy of the HOMO, and allows for a larger HOMO–LUMO gap. Finally, maps of the ESP around each cluster showed that both the tetramer and the hexamer exhibit eight regions of highly positive charge that could provide favorable binding sites for negative counteranions. Eight monovalent counterions could neutralize the tetramer but would leave the hexamer with an overall 4+ charge.

Our thermodynamic analysis suggests that although aqueous synthesis of a Zr hexamer with only water-based ligands is challenging, formation of the Zr hexamer by means of counterions or ligation may be possible. Fruitful areas for future research on this topic include an investigation of such counterion effects, and an exploration of the similarities and differences between the system studied here and aqueous hafnium clusters, which have a similar chemistry to zirconium.<sup>21,22,31,83</sup> We hope that the approach demonstrated herein will contribute to simpler and more sustainable synthesis strategies for MOFs.

## ASSOCIATED CONTENT

### Supporting Information

The Supporting Information is available free of charge at <https://pubs.acs.org/doi/10.1021/acs.inorgchem.1c02078>.

Zr clusters (ZIP)

Structures, bond lengths, and bond angles; hydrolysis Gibbs free energy methods; Pourbaix formalism methods; equilibrium constant methods; energy differences; FMOs; ESP maps; and example input files (PDF)

## AUTHOR INFORMATION

### Corresponding Author

Kristin A. Persson – Department of Materials Science and Engineering, University of California at Berkeley, Berkeley, California 94720, United States; Molecular Foundry, Lawrence Berkeley National Laboratory, Berkeley, California 94720, United States; [orcid.org/0000-0003-2495-5509](https://orcid.org/0000-0003-2495-5509); Email: [kristinpersson@berkeley.edu](mailto:kristinpersson@berkeley.edu)

### Authors

Rebecca D. Stern – Department of Materials Science and Engineering, University of California at Berkeley, Berkeley, California 94720, United States; [orcid.org/0000-0001-9942-3334](https://orcid.org/0000-0001-9942-3334)

Ryan S. Kingsbury – Department of Materials Science and Engineering, University of California at Berkeley, Berkeley, California 94720, United States; [orcid.org/0000-0002-7168-3967](https://orcid.org/0000-0002-7168-3967)

Complete contact information is available at:

<https://pubs.acs.org/doi/10.1021/acs.inorgchem.1c02078>

### Notes

The authors declare no competing financial interest.

## ACKNOWLEDGMENTS

The authors thank the Energy & Biosciences Institute through the EBI-Shell program whose funding supported this work. This research also used the Savio computational cluster resource provided by the Berkeley Research Computing program at the University of California, Berkeley (supported by the UC Berkeley Chancellor, Vice Chancellor for Research, and Chief Information Officer).

## REFERENCES

- (1) Wang, W.; Fullmer, L. B.; Bandeira, N. A. G.; Goberna-Ferrón, S.; Zakharov, L. N.; Bo, C.; Keszler, D. A.; Nyman, M. Crystallizing elusive chromium polycations. *Chem* **2016**, *1*, 887–901.
- (2) Yin, Q.; Tan, J. M.; Besson, C.; Geletii, Y. V.; Musaev, D. G.; Kuznetsov, A. E.; Luo, Z.; Hardcastle, K. I.; Hill, C. L. A fast soluble carbon-free molecular water oxidation catalyst based on abundant metals. *Science* **2010**, *328*, 342–345.

- (3) Blasco-Ahicart, M.; Soriano-López, J.; Carbó, J. J.; Poblet, J. M.; Galan-Mascaros, J. R. Polyoxometalate electrocatalysts based on earth-abundant metals for efficient water oxidation in acidic media. *Nat. Chem.* **2018**, *10*, 24–30.
- (4) Rhule, J. T.; Hill, C. L.; Judd, D. A.; Schinazi, R. F. Polyoxometalates in Medicine. *Chem. Rev.* **1998**, *98*, 327–358.
- (5) Lee, I. S.; Long, J. R.; Prusiner, S. B.; Safar, J. G. Selective precipitation of prions by polyoxometalate complexes. *J. Am. Chem. Soc.* **2005**, *127*, 13802–13803.
- (6) Anderson, J. T.; Munsee, C. L.; Hung, C. M.; Phung, T. M.; Herman, G. S.; Johnson, D. C.; Wager, J. F.; Keszler, D. A. Solution-Processed HafSOx and ZircSOx Inorganic Thin-Film Dielectrics and Nanolaminates. *Adv. Funct. Mater.* **2007**, *17*, 2117–2124.
- (7) Marsh, D. A.; Goberna-Ferrón, S.; Baumeister, M. K.; Zakharov, L. N.; Nyman, M.; Johnson, D. W. Ln polyoxocations: yttrium oxide solution speciation & solution deposited thin films. *Dalton Trans.* **2017**, *46*, 947–955.
- (8) Llordés, A.; García, G.; Gazquez, J.; Milliron, D. J. Tunable near-infrared and visible-light transmittance in nanocrystal-in-glass composites. *Nature* **2013**, *500*, 323–326.
- (9) Busche, C.; Vilà-Nadal, L.; Yan, J.; Miras, H. N.; Long, D.-L.; Georgiev, V. P.; Asenov, A.; Pedersen, R. H.; Gadegaard, N.; Mirza, M. M.; Paul, D. J.; Poblet, J. M.; Cronin, L. Design and fabrication of memory devices based on nanoscale polyoxometalate clusters. *Nature* **2014**, *515*, 545–549.
- (10) Oleksak, R. P.; Ruther, R. E.; Luo, F.; Fairley, K. C.; Decker, S. R.; Stickle, W. F.; Johnson, D. W.; Garfunkel, E. L.; Herman, G. S.; Keszler, D. A. Chemical and Structural Investigation of High-Resolution Patterning with HafSOx. *ACS Appl. Mater. Interfaces* **2014**, *6*, 2917–2921.
- (11) Castellanos Ortega, S.; Wu, L.; Baljovic, M.; Portale, G.; Kazazis, D.; Vockenhuber, M.; Ekinci, Y.; Jung, T. Ti, Zr, and Hf-based molecular hybrid materials as EUV photoresists. *Extreme Ultraviolet (EUV) Lithography IX*; SPIE, 2018; p 6.
- (12) Wills, L. A.; Qu, X.; Chang, I.-Y.; Mustard, T. J. L.; Keszler, D. A.; Persson, K. A.; Cheong, P. H.-Y. Group additivity-Pourbaix diagrams advocate thermodynamically stable nanoscale clusters in aqueous environments. *Nat. Commun.* **2017**, *8*, 15852.
- (13) Nyman, M. Encyclopedia of engineering geology. In *Encyclopedia of Earth Sciences Series*; Bobrowsky, P., Marker, B., Eds.; Springer International Publishing: Cham, 2018, pp 1–5.
- (14) Nyman, M. Polyoxoniobate chemistry in the 21st century. *Dalton Trans.* **2011**, *40*, 8049–8058.
- (15) Misra, A.; Kozma, K.; Streb, C.; Nyman, M. Beyond Charge Balance: Counter-Cations in Polyoxometalate Chemistry. *Angew. Chem.* **2020**, *59*, 596–612.
- (16) Bino, A.; Ardon, M.; Lee, D.; Spingler, B.; Lippard, S. J. Synthesis and Structure of [Fe13O4F24(OMe)12]5-: The First Open-Shell Keggin Ion. *J. Am. Chem. Soc.* **2002**, *124*, 4578–4579.
- (17) Sadeghi, O.; Zakharov, L. N.; Nyman, M. Aqueous formation and manipulation of the iron-oxo Keggin ion. *Science* **2015**, *347*, 1359–1362.
- (18) Sadeghi, O.; Falaise, C.; Molina, P. I.; Hufschmid, R.; Campana, C. F.; Noll, B. C.; Browning, N. D.; Nyman, M. Chemical stabilization and electrochemical destabilization of the iron keggion in water. *Inorg. Chem.* **2016**, *55*, 11078–11088.
- (19) Sadeghi, O.; Amiri, M.; Reinheimer, E. W.; Nyman, M. The Role of Bi 3+ in Promoting and Stabilizing Iron Oxo Clusters in Strong Acid. *Angew. Chem.* **2018**, *57*, 6247–6250.
- (20) Kondinski, A.; Monakhov, K. Y. Breaking the Gordian Knot in the Structural Chemistry of Polyoxometalates: Copper(II)-Oxo/Hydroxo Clusters. *Chem.—Eur. J.* **2017**, *23*, 7841–7852.
- (21) Sommers, J. A.; Hutchison, D. C.; Martin, N. P.; Kozma, K.; Keszler, D. A.; Nyman, M. Peroxide-Promoted Disassembly Reassembly of Zr-Polyoxocations. *J. Am. Chem. Soc.* **2019**, *141*, 16894–16902.
- (22) Kozma, K.; Zakharov, L. N.; Nyman, M. Counteranion-controlled nuclearity of Zr/Hf peroxo-oxalates. *Cryst. Growth Des.* **2020**, *20*, 6519.
- (23) Feng, L.; Pang, J.; She, P.; Li, J.-L.; Qin, J.-S.; Du, D.-Y.; Zhou, H.-C. Metal-Organic Frameworks Based on Group 3 and 4 Metals. *Adv. Mater.* **2020**, *32*, No. e2004414.
- (24) Goberna-Ferrón, S.; Park, D.-H.; Amador, J. M.; Keszler, D. A.; Nyman, M. Amphoteric aqueous hafnium cluster chemistry. *Angew. Chem.* **2016**, *55*, 6221–6224.
- (25) Molina, P. I.; Kozma, K.; Santala, M.; Falaise, C.; Nyman, M. Aqueous Bismuth Titanium-Oxo Sulfate Cluster Speciation and Crystallization. *Angew. Chem.* **2017**, *56*, 16277–16281.
- (26) Armstrong, C. R.; Casey, W. H.; Navrotsky, A. Energetics of Al<sub>13</sub> Keggin cluster compounds. *Proc. Natl. Acad. Sci. U.S.A.* **2011**, *108*, 14775–14779.
- (27) Saha, S.; Park, D. H.; Hutchison, D. C.; Olsen, M. R.; Zakharov, L. N.; Marsh, D.; Goberna-Ferrón, S.; Frederick, R. T.; Diulus, J. T.; Kenane, N.; Herman, G. S.; Johnson, D. W.; Keszler, D. A.; Nyman, M. Alkyltin keggion clusters templated by sodium. *Angew. Chem.* **2017**, *56*, 10140–10144.
- (28) Hutchison, D. C.; Stern, R. D.; Olsen, M. R.; Zakharov, L. N.; Persson, K. A.; Nyman, M. Alkyltin clusters: the less symmetric Keggin isomers. *Dalton Trans.* **2018**, *47*, 9804–9813.
- (29) Sures, D.; Segado, M.; Bo, C.; Nyman, M. Alkali-Driven Disassembly and Reassembly of Molecular Niobium Oxide in Water. *J. Am. Chem. Soc.* **2018**, *140*, 10803–10813.
- (30) Chen, D.; Yang, D.; Dougherty, C. A.; Lu, W.; Wu, H.; He, X.; Cai, T.; Van Dort, M. E.; Ross, B. D.; Hong, H. In Vivo Targeting and Positron Emission Tomography Imaging of Tumor with Intrinsically Radioactive Metal-Organic Frameworks Nanomaterials. *ACS Nano* **2017**, *11*, 4315–4327.
- (31) Yuan, S.; Qin, J.-S.; Lollar, C. T.; Zhou, H.-C. Stable Metal-Organic Frameworks with Group 4 Metals: Current Status and Trends. *ACS Cent. Sci.* **2018**, *4*, 440–450.
- (32) Rimoldi, M.; Howarth, A. J.; DeStefano, M. R.; Lin, L.; Goswami, S.; Li, P.; Hupp, J. T.; Farha, O. K. Catalytic Zirconium/Hafnium-Based Metal-Organic Frameworks. *ACS Catal.* **2017**, *7*, 997–1014.
- (33) Pakamoré, I.; Rousseau, J.; Rousseau, C.; Monflier, E.; Szilágyi, P. A. An ambient-temperature aqueous synthesis of zirconium-based metal-organic frameworks. *Green Chem.* **2018**, *20*, 5292–5298.
- (34) James, S. L.; et al. Mechanochemistry: opportunities for new and cleaner synthesis. *Chem. Soc. Rev.* **2012**, *41*, 413–447.
- (35) Užarević, K.; Wang, T. C.; Moon, S.-Y.; Fidelli, A. M.; Hupp, J. T.; Farha, O. K.; Friščić, T. Mechanochemical and solvent-free assembly of zirconium-based metal-organic frameworks. *Chem. Commun.* **2016**, *52*, 2133–2136.
- (36) Cavka, J. H.; Jakobsen, S.; Olsbye, U.; Guillou, N.; Lamberti, C.; Bordiga, S.; Lillerud, K. P. A new zirconium inorganic building brick forming metal organic frameworks with exceptional stability. *J. Am. Chem. Soc.* **2008**, *130*, 13850–13851.
- (37) Clearfield, A.; Vaughan, P. A. The crystal structure of zirconyl chloride octahydrate and zirconyl bromide octahydrate. *Acta Crystallogr.* **1956**, *9*, 555–558.
- (38) Muha, G. M.; Vaughan, P. A. Structure of the complex ion in aqueous solutions of zirconyl and hafnium oxyhalides. *J. Chem. Phys.* **1960**, *33*, 194–199.
- (39) Mak, T. C. W. Refinement of the crystal structure of zirconyl chloride octahydrate. *Can. J. Chem.* **1968**, *46*, 3491–3497.
- (40) Maestre, J.; Poblet, J.; Bo, C.; Casan-Pastor, N.; Gomez-Romero, P. Electronic Structure of the Highly Reduced Polyoxoanion [PMo12O40(VO)2]5-: A DFT Study. *Inorg. Chem.* **1998**, *37*, 3444.
- (41) López, X.; Maestre, J. M.; Bo, C.; Poblet, J.-M. Electronic Properties of Polyoxometalates: A DFT Study of  $\alpha/\beta$ -[XM12O40]n- Relative Stability (M = W, Mo and X a Main Group Element). *J. Am. Chem. Soc.* **2001**, *123*, 9571–9576.
- (42) López, X.; Bo, C.; Poblet, J. M. Electronic properties of polyoxometalates: electron and proton affinity of mixed-addenda Keggin and Wells-Dawson anions. *J. Am. Chem. Soc.* **2002**, *124*, 12574–12582.

- (43) López, X.; Poblet, J. M. DFT Study on the Five Isomers of PW12O40<sup>3-</sup>: Relative Stabilization upon Reduction. *Inorg. Chem.* **2004**, *43*, 6863–6865.
- (44) Fernández, J. A.; López, X.; Poblet, J. M. A DFT study on the effect of metal, anion charge, heteroatom and structure upon the relative basicities of polyoxoanions. *J. Mol. Catal. A: Chem.* **2007**, *262*, 236–242.
- (45) López, X.; Miró, P.; Carbó, J. J.; Rodríguez-Forteza, A.; Bo, C.; Poblet, J. M. Current trends in the computational modelling of polyoxometalates. *Theor. Chem. Acc.* **2011**, *128*, 393–404.
- (46) López, X.; Carbó, J. J.; Bo, C.; Poblet, J. M. Structure, properties and reactivity of polyoxometalates: a theoretical perspective. *Chem. Soc. Rev.* **2012**, *41*, 7537–7571.
- (47) André Ohlin, C.; Rustad, J. R.; Casey, W. H. The energetics of isomerisation in Keggin-series aluminate cations. *Dalton Trans.* **2014**, *43*, 14533–14536.
- (48) Sulpizi, M.; Lützenkirchen, J. Atypical titration curves for GaAl12 Keggin-ions explained by a joint experimental and simulation approach. *J. Chem. Phys.* **2018**, *148*, 222836.
- (49) Das, B. Theoretical Study of Small Iron-Oxyhydroxide Clusters and Formation of Ferrihydrite. *J. Phys. Chem. A* **2018**, *122*, 652–661.
- (50) Rao, N.; Holerca, M. N.; Klein, M. L.; Pophristic, V. Computational study of the Zr<sup>4+</sup> tetranuclear polymer, [Zr<sub>4</sub>(OH)<sub>8</sub>(H<sub>2</sub>O)<sub>16</sub>]<sup>8+</sup>. *J. Phys. Chem. A* **2007**, *111*, 11395–11399.
- (51) Rao, N.; Holerca, M. N.; Pophristic, V. Computational study of the small zirconium polynuclear species. *J. Chem. Theory Comput.* **2008**, *4*, 145–155.
- (52) Sasaki, T.; Kobayashi, T.; Takagi, I.; Moriyama, H. Hydrolysis constant and coordination geometry of zirconium(IV). *J. Nucl. Sci. Technol.* **2008**, *45*, 735–739.
- (53) Jansen van Vuuren, D. B.; Krieg, H. M.; van Sittert, C. G. C. E. Computational chemistry study of zirconium monomers in low acid concentration aqueous solutions. *IOP Conf. Ser.: Mater. Sci. Eng.* **2018**, *430*, 012017.
- (54) Patel, A. M.; Nørskov, J. K.; Persson, K. A.; Montoya, J. H. Efficient Pourbaix diagrams of many-element compounds. *Phys. Chem. Chem. Phys.* **2019**, *21*, 25323–25327.
- (55) Singh, A. K.; Montoya, J. H.; Gregoire, J. M.; Persson, K. A. Robust and synthesizable photocatalysts for CO<sub>2</sub> reduction: a data-driven materials discovery. *Nat. Commun.* **2019**, *10*, 443.
- (56) Newhouse, P. F.; Reyes-Lillo, S. E.; Li, G.; Zhou, L.; Shinde, A.; Guevarra, D.; Suram, S. K.; Soedarmadji, E.; Richter, M. H.; Qu, X.; Persson, K.; Neaton, J. B.; Gregoire, J. M. Discovery and Characterization of a Pourbaix-Stable, 1.8 eV Direct Gap Bismuth Manganate Photoanode. *Chem. Mater.* **2017**, *29*, 10027–10036.
- (57) Shinde, A.; Suram, S. K.; Yan, Q.; Zhou, L.; Singh, A. K.; Yu, J.; Persson, K. A.; Neaton, J. B.; Gregoire, J. M. Discovery of Manganese-Based Solar Fuel Photoanodes via Integration of Electronic Structure Calculations, Pourbaix Stability Modeling, and High-Throughput Experiments. *ACS Energy Lett.* **2017**, *2*, 2307–2312.
- (58) Persson, K. A.; Waldwick, B.; Lazic, P.; Ceder, G. Prediction of solid-aqueous equilibria: Scheme to combine first-principles calculations of solids with experimental aqueous states. *Phys. Rev. B: Condens. Matter Phys.* **2012**, *85*, 235438.
- (59) Singh, A. K.; Zhou, L.; Shinde, A.; Suram, S. K.; Montoya, J. H.; Winston, D.; Gregoire, J. M.; Persson, K. A. Electrochemical stability of metastable materials. *Chem. Mater.* **2017**, *29*, 10159–10167.
- (60) Jain, A.; Ong, S. P.; Hautier, G.; Chen, W.; Richards, W. D.; Dacek, S.; Cholia, S.; Gunter, D.; Skinner, D.; Ceder, G.; Persson, K. A. Commentary: The Materials Project: A materials genome approach to accelerating materials innovation. *APL Mater.* **2013**, *1*, 011002.
- (61) Frisch, M. J.; et al. *Gaussian 16*, Revision A.03; Gaussian Inc: Wallingford CT, 2016.
- (62) Becke, A. D. Density-functional thermochemistry. III. The role of exact exchange. *J. Chem. Phys.* **1993**, *98*, 5648.
- (63) Hariharan, P. C.; Pople, J. A. The influence of polarization functions on molecular orbital hydrogenation energies. *Theor. Chim. Acta* **1973**, *28*, 213–222.
- (64) Wadt, W. R.; Hay, P. J. Ab initio effective core potentials for molecular calculations. Potentials for main group elements Na to Bi. *J. Chem. Phys.* **1985**, *82*, 284–298.
- (65) Kreutzer, J.; Blaha, P.; Schubert, U. Assessment of different basis sets and DFT functionals for the calculation of structural parameters, vibrational modes and ligand binding energies of Zr<sub>4</sub>O<sub>2</sub> (carboxylate)<sub>12</sub> clusters. *Comput. Theor. Chem.* **2016**, *1084*, 162–168.
- (66) Yang, Y.; Weaver, M. N.; Merz, K. M. Assessment of the “6-31+G\*\* + LANL2DZ” mixed basis set coupled with density functional theory methods and the effective core potential: prediction of heats of formation and ionization potentials for first-row-transition-metal complexes. *J. Phys. Chem. A* **2009**, *113*, 9843–9851.
- (67) Klamt, A.; Schüürmann, G. COSMO: a new approach to dielectric screening in solvents with explicit expressions for the screening energy and its gradient. *J. Chem. Soc., Perkin Trans. 2* **1993**, 799–805.
- (68) Balogh, E.; Anderson, T. M.; Rustad, J. R.; Nyman, M.; Casey, W. H. Rates of oxygen-isotope exchange between sites in the [HxTa<sub>6</sub>O<sub>19</sub>](8-x)<sup>-</sup>(aq) Lindqvist ion and aqueous solutions: comparisons to [HxNb<sub>6</sub>O<sub>19</sub>](8-x)<sup>-</sup>(aq). *Inorg. Chem.* **2007**, *46*, 7032–7039.
- (69) Krishnan, R.; Binkley, J. S.; Seeger, R.; Pople, J. A. Self-consistent molecular orbital methods. XX. A basis set for correlated wave functions. *J. Chem. Phys.* **1980**, *72*, 650.
- (70) O’Boyle, N. M.; Tenderholt, A.; Langner, K. A library for package-independent computational chemistry algorithms. *J. Comput. Chem.* **2008**, *29*, 839–845.
- (71) Sundstrom, E. J.; Yang, X.; Thoi, V. S.; Karunadasa, H. I.; Chang, C. J.; Long, J. R.; Head-Gordon, M. Computational and experimental study of the mechanism of hydrogen generation from water by a molecular molybdenum-oxo electrocatalyst. *J. Am. Chem. Soc.* **2012**, *134*, 5233–5242.
- (72) Casanovas, R.; Ortega-Castro, J.; Frau, J.; Donoso, J.; Muñoz, F. Theoretical pK<sub>a</sub> calculations with continuum model solvents, alternative protocols to thermodynamic cycles. *Int. J. Quantum Chem.* **2014**, *114*, 1350–1363.
- (73) Ong, S. P.; Richards, W. D.; Jain, A.; Hautier, G.; Kocher, M.; Cholia, S.; Gunter, D.; Chevrier, V. L.; Persson, K. A.; Ceder, G. Python Materials Genomics (pymatgen): A robust, open-source python library for materials analysis. *Comput. Mater. Sci.* **2013**, *68*, 314–319.
- (74) Hagfeldt, C.; Kessler, V.; Persson, I. Structure of the hydrated, hydrolysed and solvated zirconium(IV) and hafnium(IV) ions in water and aprotic oxygen donor solvents. A crystallographic, EXAFS spectroscopic and large angle X-ray scattering study. *Dalton Trans.* **2004**, 2142–2151.
- (75) Hennig, C.; Weiss, S.; Kraus, W.; Kretzschmar, J.; Scheinost, A. C. Solution species and crystal structure of zirconium(IV) acetate. *Inorg. Chem.* **2017**, *56*, 2473–2480.
- (76) Singhal, A.; Toth, L. M.; Lin, J. S.; Affholter, K. Zirconium(IV) tetramer/octamer hydrolysis equilibrium in aqueous hydrochloric acid solution. *J. Am. Chem. Soc.* **1996**, *118*, 11529–11534.
- (77) Brown, P. L.; Curti, E.; Grambow, B.; Ekberg, C.; Mompean, F. J.; Perrone, J.; Illemassene, M. *Chemical Thermodynamics of Zirconium*, 1st ed.; Elsevier, 2005; Vol. 8, pp 544.
- (78) Wang, W.; Wentz, K. M.; Hayes, S. E.; Johnson, D. W.; Keszler, D. A. Synthesis of the hydroxide cluster [Al<sub>13</sub>(3-OH)<sub>6</sub>(-OH)<sub>18</sub>(H<sub>2</sub>O)<sub>24</sub>]<sup>15+</sup> from an aqueous solution. *Inorg. Chem.* **2011**, *50*, 4683–4685.
- (79) Koole, R.; Groeneveld, E.; Vanmaekelbergh, D.; Meijerink, A.; de Mello Donegá, C. Size Effects on Semiconductor Nanoparticles. *Workhorses of Nanoscience*, 1st ed.; Springer-Verlag Berlin Heidelberg, 2014; pp 13–51.
- (80) Pan, L.; Heddy, R.; Li, J.; Zheng, C.; Huang, X.-Y.; Tang, X.; Kilpatrick, L. Synthesis and structural determination of a hexanuclear zirconium glycine compound formed in aqueous solution. *Inorg. Chem.* **2008**, *47*, 5537–5539.

(81) Huelsenbeck, L.; Luo, H.; Verma, P.; Dane, J.; Ho, R.; Beyer, E.; Hall, H.; Geise, G. M.; Giri, G. Generalized approach for rapid aqueous MOF synthesis by controlling solution pH. *Cryst. Growth Des.* **2020**, *20*, 6787–6795.

(82) Xu, H.; Sommer, S.; Broge, N. L. N.; Gao, J.; Iversen, B. B. The Chemistry of Nucleation: In Situ Pair Distribution Function Analysis of Secondary Building Units During UiO-66 MOF Formation. *Chem.—Eur. J.* **2019**, *25*, 2051–2058.

(83) Sommers, J. A.; Hutchison, D. C.; Martin, N. P.; Palys, L.; Amador, J. M.; Keszler, D. A.; Nyman, M. Differentiating Zr/HfIV Aqueous Polyoxocation Chemistry with Peroxide Ligation. *Inorg. Chem.* **2021**, *60*, 1631.